Bidirectional reflectance of oceanic waters: accounting for Raman emission and varying particle scattering phase function

André Morel, David Antoine, and Bernard Gentili

The bidirectionality of the upward radiance field in oceanic case 1 waters has been reinvestigated by incorporation of revised parameterizations of inherent optical properties as a function of the chlorophyll concentration (Chl), considering Raman scattering and making the particle phase function shape ($\tilde{\beta}_p$) continuously varying along with the Chl. Internal consistency is thus reached, as the decrease in backscattering probability (for increasing Chl) translates into a correlative change in $\tilde{\beta}_p$. The single particle phase function (previously used) precluded a realistic assessment of bidirectionality for waters with Chl > 1 mg m^{-3}. This limitation is now removed. For low Chl, Raman emissions significantly affect the radiance field. For moderate Chl (0.1–1 mg m^{-3}), new and previous bidirectional parameters remain close. The ocean reflectance anisotropy has implications in ocean color remote-sensing problems, in derivation of coherent water-leaving radiances, in associated calibration–validation activities, and in the merging of data obtained under various geometrical configurations. © 2002 Optical Society of America

OCIS codes: 010.4450, 290.5840, 290.5850, 290.5860, 290.4210.

1. Introduction

In general, the upward radiance field beneath the ocean surface, and therefore the emerging radiance field, is not isotropic. This bidirectional structure of the in-water radiative field results from the nonisotropic character of the volume scattering function (VSF) of the water body, combined with nonisotropic illumination conditions generally prevailing above the surface. This phenomenon can be theoretically studied by solution of the radiative transfer equation (RTE) for the coupled atmosphere–ocean system. The variations in the bidirectional properties of the upward radiative field have already been reported for case 1 waters and related to the chlorophyll concentration (Chl) (Morel and Gentili[1–3]; these papers are thereafter referred to as MG-91, MG-93, and MG-96). Some of these theoretical findings were corroborated by field measurements made by Voss by using an underwater camera system[4] in low-chlorophyll case 1 waters to accurately assess the upward radiance field.[5] The extent of the variations in the angular structure of the upward radiative stream as a function of the Sun's position was confirmed[5] by these data. Similar predictive investigations[6] were tentatively extended to typical case 2 waters, either dominated by sediment or by colored dissolved organic compounds, without having been verified in natural environments.

The VSF is of prime importance in shaping the radiance fields; the backward lobe of this function is particularly involved in ruling the angular pattern of the upward field. Water molecules and suspended particles contribute to the scattering process, but with drastically differing phase functions. Therefore the shape of the resulting VSF of seawater depends on the respective proportions of the two types of scatterer. By accounting for the fact that, in most oceanic waters, molecular scattering is definitely not negligible compared with particle scattering, MG-91, the first paper, examined the impact on ocean bidirectional reflectance of varying proportions between the two types of scatterer.

Although molecular scattering is well known with regard to its magnitude, angular pattern, and spectral dependency, particle scattering has been much less studied. The natural variability in the shape of

The authors are with the Laboratoire d'Océanographie de Villefranche, Université Pierre et Marie Curie and Centre National de la Recherche Scientifique, Villefranche-sur-Mer, France. A. Morel's e-mail address is morel@obs-vlfr.fr.

Received 25 February 2002; revised manuscript received 5 July 2002.

0003-6935/02/306289-18$15.00/0

© 2002 Optical Society of America

the particle VSF, in particular for the backward directions (backscattering), remains up to now scarcely documented. Therefore assumptions were necessary for the previous computations. They consisted of adopting a unique normalized VSF for all sorts of oceanic particle, whatever the Chl. This particulate phase function was that derived from Petzold's measurements[7] (as used by Mobley *et al.*[8] and other investigators, for instance, Kirk[9] and Gordon[10]). Nevertheless, the adoption of such a single-particulate phase function remains undoubtedly a weakness, which was already acknowledged in MG-91 (their Fig. 4) and repeatedly emphasized thereafter (MG-93 and MG-96).

The specific motivations for the present study are as follows. The Petzold phase function results in a constant backscattering probability $\tilde{b}_{bp}$ (i.e., b_{bp}/b_p, the ratio of backscattering to scattering by particles) of 1.9%. This high value contradicts indirect observations (via reflectance determinations) that tend to demonstrate that only much lower values can explain the observed reflectance in oceanic waters, particularly when the Chl becomes high (see Fig. 1). Such a $\tilde{b}_{bp}$ value is also incompatible with more realistic, empirical parameterizations, by which the backscattering probability is allowed to decrease when the Chl increases, as proposed in Gordon *et al.*,[12] Morel,[13] and Ulloa *et al.*[14] or recently by Twardowski *et al.*[15] and Morel and Maritorena[11] [see Eq. (1) below]. Owing to this well-identified weakness, the results regarding the bidirectional reflectance properties (MG-91, MG-93, and MG-96) were considered as becoming dubious when the Chl exceeds approximately 1 mg m^{-3}. Indeed, in such cases, particle scattering predominates, and thus the high $\tilde{b}_{bp}$ value (and the related particle backscattering lobe) crucially affects the results. The same statement holds true for any other predicted apparent optical properties in chlorophyll-rich waters, as long as the backward lobe of the particle phase function is not appropriately represented.

One specific aim of the present paper is to try to remove the previously acknowledged weakness and thus to derive the bidirectional parameters for an extended Chl range. If an empirical model accounts for a continuous change in $\tilde{b}_{bp}$ along with the Chl (actually a decrease for increasing Chl), this must translate into a correlative change in the shape of the particle phase function. Only under this proviso can the consistency of radiative transfer computations be ensured. The present paper deals with only one of the apparent optical properties, namely, the bidirectional reflectance of the upper oceanic layer, obviously one of the most sensitive to the shape of the backward lobe of the phase function.

Moreover, most oceanic waters are rather oligotrophic (i.e., with a low Chl) and, accordingly, with a low suspended matter content. As a consequence, in such clear waters, the signal originating from elastic particle backscattering is rather reduced, so that the inelastic Raman scattering can no longer be neglected. The present study considers and includes this effect. Finally, the biogeochemical variables derived from the remote sensing of the ocean color are based on the determination from space of the water-leaving radiance. Therefore the practical application of the present study is to provide tools for correcting these radiances in order to derive and possibly merge comparable and meaningful radiometric quantities, free from such bidirectional effects.

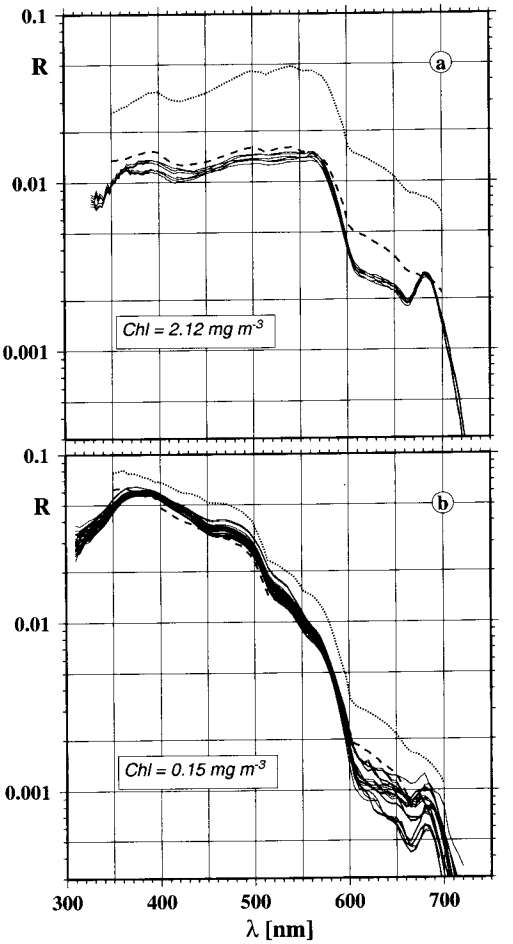

Fig. 1. Spectral irradiance reflectance below the surface in oceanic waters with two differing Chls, as indicated. Solid curves, field determinations; dashed curves, modeled values (Morel and Maritorena[11]); and dotted curves, modeled values when the backscattering efficiency is given the constant value 1.9% (derived from Petzold phase function) instead of that derived from Eq. (1). (a) 9 September 1999, Atlantic Ocean, Moroccan upwelling area (10.02 °W, 31.01 °N); (b) 18–22 November 1994, Pacific Ocean (150 °W, 5 °S). Note that the chlorophyll fluorescence peak, around 683 nm, clearly seen in the measured reflectances, is not modeled.

2. Theoretical and Computational Aspects

A. Parameterization of the Particle Phase Function for Oceanic Surface Waters

Although the trend during recent years has been to adopt a single (the Petzold) phase function for all kinds of marine particle (mainly for the sake of intercomparability between various RTE computations

and simulations), approaches some decades ago were different and envisaged the coexistence of several particle populations with differing phase functions (see, e.g., Gordon and Brown[16]; Brown and Gordon[17]; and Zaneveld *et al.*[18]). Russian opticists remained in favor of a two-component model, as developed by Kopelevich[19] (see also Shifrin[20]); an overview of the Kopelevich–Haltrin model was provided by Mobley.[21] Basically, this model cumulates the contributions of so-called small and large particles in varying proportions.

The small fraction includes mineral particles (size < 1 μm) with an index of refraction $n_s = 1.15$ (relative to water), whereas the large fraction consists of biological particles (>1 μm) with a relative index $n_1 = 1.03$. Each fraction has its own specific phase function (Table 3.13 of Mobley[21]). The relative contributions of each fraction are either related to the total scattering coefficient (Kopelevich[19]) or parameterized in terms of Chl (Haltrin and Kattawar[22]). Somewhat surprisingly, in this model, the relative concentration of small particles increases when the Chl increases, which disagrees with the common observation of a decreasing relative abundance of small particles in case 1 waters when the algal content increases. The fact that the population of small particles would be purely mineral also seems questionable, at least in case 1 waters, and within upper layers, in which picoplankton, heterotrophic bacteria, viruses, and organic debris are known to be abundant in this size range (see, e.g., Stramski and Kiefer[23]).

According to the Russian model, the backscattering probabilities for the small- and large-particle populations are 3.9% and 0.064%, respectively. The mixtures, made with varying proportions according to the Chl, exhibit $\tilde{b}_{bp}$ values that vary from approximately 0.92% to 1.17% when the Chl increases from 0.03 to 3 mg m^{-3} [Eq. (3.45) of Mobley[21] and the present Fig. 2]. Actually, when the phase functions proposed for the mixtures [Eq. (3.38) and Table 3.13 of Mobley[21]] are integrated, other figures are obtained for $\tilde{b}_{bp}$ that are higher than those mentioned above and are also greater at high Chl (Fig. 2).

The objective here is to develop a parameterization of the particle phase function able to progressively change with the Chl value, in such a way that the backscattering efficiency can decrease with increasing Chl, according to

$$b_{bp}/b_p = \tilde{b}_{bp} = 0.002 + \{0.01[0.5 - 0.25 \log_{10}(\mathrm{Chl})]\}. \quad (1)$$

This empirical parameterization, proposed by Morel and Maritorena,[11] accounts well for the irradiance reflectance determined at sea for a wide range of Chl (see Fig. 10 of Ref. 11 and the present Fig. 1).

In a way similar to that adopted by Kopelevich, the desired phase function is also obtained as a mixture of two functions that are separately computed for populations dominated either by small, or by large particles. It has been postulated that for both populations the number size distribution, $N(x)$, obeys a Junge law, as

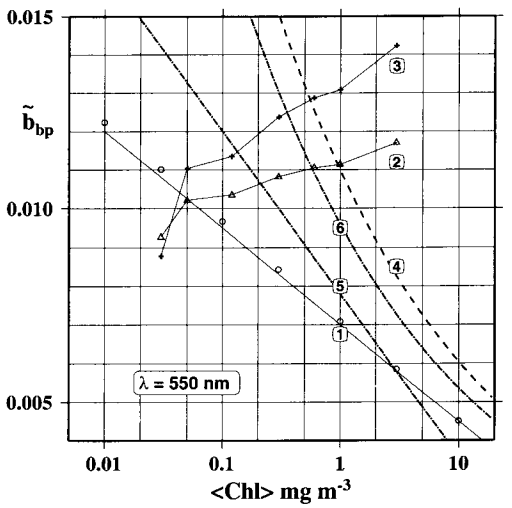

Fig. 2. Backscattering probability of marine particles as a function of the Chl. Curve 1, from Eq. (1), and the superimposed circles derived from the phase functions shown in Fig. 3(a), by appropriate integration; curve 2, from the Kopelevich–Haltrin–Kattawar model [namely, from Eqs. (3.43) and (3.45), and Table 3.14 of Mobley[21]]; curve 3, also from the Russian model by integration of the particle phase functions [Eq. (3.38) and Table 3.13 of Mobley[21]]; curve 4, from Gordon *et al.*[12]; curve 5, from Twardowski *et al.*[15]; and curve 6, from Ulloa *et al.*[14]

$$N(x) = Kx^{-j}, \quad (2)$$

where x represents the size (an effective diameter), $N(x)dx$ is the number of particles in the size interval from x to $x + dx$, and K sets the numerical abundance. The two populations differ by their exponents, namely, $j = 4.2$ and 3.1, but not by their nature, assumed to be organic for the large particles as well as for the small particles (see below). With a value equal to 4.2, the numerical abundance of the small particles is considerably enhanced compared with that of the population of large particles with $j = 3.1$. As a consequence (see Fig. 9 of Morel and Maritorena[11]), the backscattering probability for a given refractive index is higher for the small-particle population than for the large particles. It is conceivable that mixtures of both populations may be built in order to follow a continuous change in $\tilde{b}_{bp}$, as prescribed by Eq. (1).

Another assumption, about the index of refraction (relative to that of water), is necessary to carry out computations. In contrast to the choice made by the Russian school, it has been considered here that in open ocean case 1 waters, and particularly within the upper layer, the suspended material is essentially of organic origin (living or detritus) with a low relative index (say, 1.06 ± 0.04; Aas[24]) and that mineral particles (such as aeolian dust[25]) remain exceptions and do not appreciably affect the bulk index (note that this statement would not hold true for coccoliths-dominated waters). Therefore the two populations, differing by their size distribution, will be given a

similar low refractive index (actually, identical indices, for numerical convenience; see below).

The well-known problem with spheres (particularly for low j values, when large-size particles are abundantly represented) is the development of rainbows within the phase function, the position of which depends on the refractive index. Also with spheres, a sharp peak develops in the backward direction (around 180°, owing to perpendicular reflection). To reduce these undesirable effects, we have abandoned the assumption of spheres and the use of the Mie calculation in our computations. Randomly oriented spheroidal particles (oblate and prolate, with shape factors of 3/2 and 2/3) have been considered, and the T-matrix method, as operationally developed by Mishchenko,[26] has been used to compute the individual scattering function for each size considered. It is absolutely not claimed that spheroids mimic the natural particles in a better way; however, they have the advantage of eliminating most of the scattering peculiarities ensued from sphericity, in the backward directions in particular. Because the computations for spheroids become excessively lengthy for large particles (or even become unfeasible), only one set of computations, which uses a single index, namely, 1.06, has been carried out. The size limits approximately correspond to particles ranging from 0.02 to 14 μm (diameter of equivalent spheres with equal geometrical cross sections). Therefore the same particles were used to build the two populations, which thus differ only by their size distribution. The scattering functions computed for individual particles were added with the weights corresponding to their numerical abundance provided by Eq. (2) and with $j = 3.1$ and 4.2. The VSFs are then normalized by their integrals to obtain the two phase functions shown in Fig. 3(a).

The corresponding backscattering probabilities derived from these two phase functions are 1.40% and 0.19% for small and large particles, respectively. The phase function of mixed populations, which comprise small and large particles, are operationally computed through a linear combination [see Fig. 3(a)]:

$$\tilde{\beta}_p(\psi, \mathrm{Chl}) = \alpha_s(\mathrm{Chl})\tilde{\beta}_{p,s}(\psi) + \alpha_l(\mathrm{Chl})\tilde{\beta}_{p,l}(\psi), \quad (3)$$

where ψ denotes the scattering angle, the subscripts s and l stand for small and large particles, respectively (and p for particles), and the coefficients α_s and α_l are such that

$$\alpha_s + \alpha_l = 1, \quad (4)$$

where α_s is related to the decimal logarithm of the Chl (within the range $0.1 < \mathrm{Chl} < 10$ mg m^{-3}) through

$$\alpha_s(\mathrm{Chl}) = 0.855[0.5 - 0.25 \log_{10}(\mathrm{Chl})]. \quad (5)$$

This equation states that the relative role of the small-particle population decreases when the Chl increases. Such an evolution is consistent with the observation of a relationship between phytoplankton size and abundance; indeed, picoplankton dominate in oligotrophic conditions, whereas, large cells generally develop in bloom situations. The same mixing rule [Eqs. (3)–(5)] also applies to the backscattering probabilities, so that, with the end-member values above (1.40% and 0.19%), the $\tilde{b}_{bp}$ variations expressed by Eq. (1) are well reproduced (Fig. 2). Note that the weighing coefficients α_s and α_l do not represent in a straightforward fashion the Chl or the volume concentration within each population.

The resulting phase functions for various Chls are shown in Fig. 3(a), in which the initial phase functions (for pure small- and large-particle populations) are also displayed, together with their mixtures [Eq. (3)]. The shape of these phase functions are not made wavelength dependent. The global phase

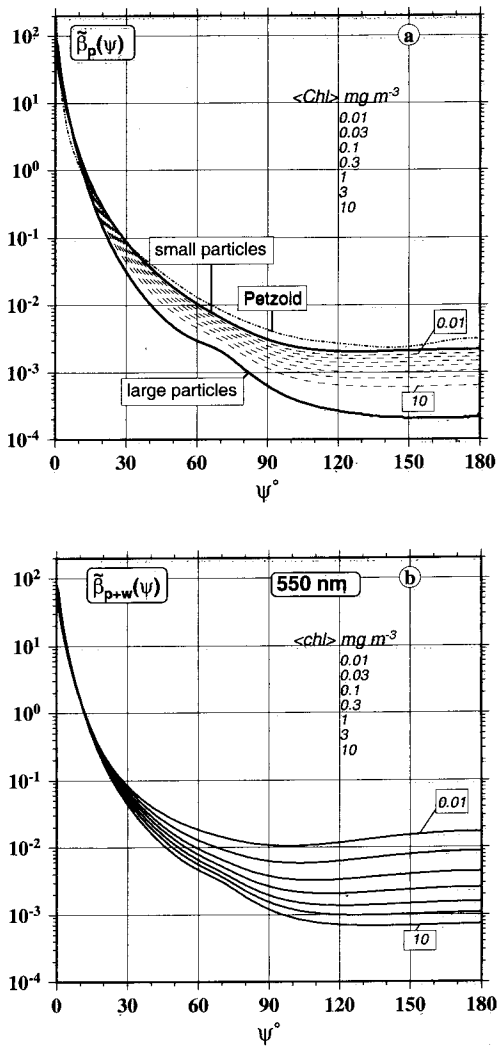

Fig. 3. (a) Phase functions for the populations of small and large particles (see text); in between, phase functions for their mixtures varying along with the Chl, according to Eqs. (3)–(5). The particle phase function derived[21] from Petzold's measurements[7] is also displayed. (b) Global phase functions at $\lambda = 550$ nm [Eq. (6)] merging molecular and particle scattering for various Chls, as indicated.

functions for oceanic waters (at $\lambda = 550$ nm) that account for both particle scattering and molecular scattering are displayed in Fig. 3(b). They are obtained through

$$\tilde{\beta}_{p+w}(\psi, \mathrm{Chl}) = [b_p(\mathrm{Chl})\tilde{\beta}_p(\psi, \mathrm{Chl}) + b_w\tilde{\beta}_w(\psi)]/[b_p(\mathrm{Chl}) + b_w], \quad (6)$$

where

$$b_w(550) = 1.93 \times 10^{-4}\ \mathrm{m}^{-1},$$
$$\tilde{\beta}_w(\psi) = \{3/[4\pi(3 + p)]\}[1 + p\ \cos^2(\psi)], \quad (7)$$

with $p = 0.84$ (Morel[27]),

$$b_p(550, \mathrm{Chl}) = 0.416(\mathrm{Chl})^{0.766} \quad (8)$$

(Loisel and Morel[28]).

The particle scattering coefficient, $b_p(\lambda, \mathrm{Chl})$, is assumed to depend on the wavelength, as explicited below [Eq. (14)]. The pure-water scattering coefficient is spectrally varying according to[27]

$$b_w(\lambda) = b_w(550)(\lambda/550)^{-4.3}.$$

The wavelength dependency of the global phase functions is thus produced through the scattering coefficients (b_p and b_w), which are used as weighing coefficients in Eq. (6).

B. Bidirectional Properties, Slant Radiance, and Normalized Radiance

The basic quantities and equations related to the bidirectional properties can be found in MG-96. The geometry, symbols, and angles are as in Fig. 1 of MG-96. A minimum set of definitions and relations is presented below, for the sake of completeness. The fundamental equation below [Eq. (9)] relates any slant radiance exiting the water, $L_w(0^+)$, to the downwelling irradiance (E_d) just above the surface (symbol 0^+) and to the absorption and backscattering coefficients of the water body (a and b_b) through three quantities $\Re$, f, and Q:

$$L_w(0^+, \theta_s, \tau_a, W, \theta, \phi, \lambda, \mathrm{IOP}) = E_d(0^+, \theta_s, \tau_a, \lambda) \times \Re(\theta', W)\frac{f(\theta_s, \tau_a, W, \mathrm{IOP})}{Q(\theta_s, \tau_a, W, \theta', \phi, \mathrm{IOP})}\left(\frac{b_b}{a}\right). \quad (9)$$

This radiance, at a given wavelength λ, depends on its own direction (depicted by θ, the zenith angle, and ϕ, the azimuthal angular distance from the Sun's direction), on the illumination conditions (summarized by the solar zenith angle, θ_s, and τ_a, the aerosol optical thickness), and on the sea state (via the wind speed, W). The illumination conditions (θ_s, and τ_a) also determine the spectral downward irradiance E_d. Inherent optical property is denoted IOP. The definition of the three quantities (Q, f, and $\Re$), which appear in Eq. (9), are briefly recalled here.

The bidirectional function Q, defined as

$$Q = E_u(0^-)/L_u(0^-, \theta', \phi), \quad (10)$$

is the ratio of upward irradiance (at null depth and just beneath the surface, denoted 0^-) to the in-water slant upward radiance L_u (also at 0^-), which gives rise to $L_w(0^+)$ after having emerged. The nadir angle, θ', is related to θ through Snell's law ($\sin\theta = n \sin\theta'$, where $n = 1.34$ is the refractive index of seawater). Note that, were L_u constant whatever the angles θ' and ϕ, Q would equal π sr. That is not generally the case, and Q actually is a bidirectional function [full expression in Eq. (9)] depending on the angular configuration (θ_s, θ', and ϕ) and environmental factors; in addition, Q also depends on the water body's IOPs, particularly on its VSF.

The dimensionless coefficient f, which regulates the magnitude of the irradiance reflectance, appears through the relationship

$$R = E_u(0^-)/E_d(0^-) = f(b_b/a). \quad (11)$$

Thus f relates the irradiance reflectance, E_u/E_d, to the IOP, namely, to the ratio b_b/a. If b_b is not small with respect to a, it is better to use the coefficient f' that relates R to the ratio $b_b/(a + b_b)$. These coefficients, f or f', depend on the IOPs and on external conditions (θ_s, τ_a, and W), as explicited in Eq. (9).

Finally, the dimensionless factor, $\Re$, which essentially depends on θ' and on wind speed (weakly on θ_s for $\theta_s < 70°$), merges all the reflection and refraction effects that occur when downward irradiance and upward radiance propagate through the wavy interface (MG-96). It depends on the refractive index of seawater and on the statistics of the capillary-wave slopes but not on the IOPs. For small θ' values ($<15°$), it amounts to 0.53 and is rather insensitive to the wind speed (Fig. 11 of MG-96); in contrast, it decreases and depends heavily on W when θ' increases toward the critical angle, θ_c (see Fig. 4).

The bidirectional structure of the upward field formed by the radiances leaving the ocean surface is of crucial importance when remotely sensed ocean color data is interpreted. For instance, the radiances exiting a homogeneous ocean, seen under various angles and differing illumination conditions, are not constant. As a consequence, the consistency of spectral radiance data, derived from space observation under varying illumination and viewing geometries (even under the assumption of a perfect atmospheric correction), is not straightforward, as long as these geometrical effects have not been removed. Yet such a consistency is a prerequisite when various pixels observed within a swath, or along the orbit, or viewed during successive days, or by various sensors in flight, are to be compared. Merging the radiance data captured by several instruments operating simultaneously, which is one of the goals of the Sensor Intercomparison and Merger for Biological and Interdisciplinary Oceanic Studies project, requires that such an internal consistency be achieved.

The concept of spectral "normalized water-leaving radiance," denoted $[L_w(\lambda)]_n$, originally introduced by Gordon and Clark,[29] was an attempt at fulfilling this

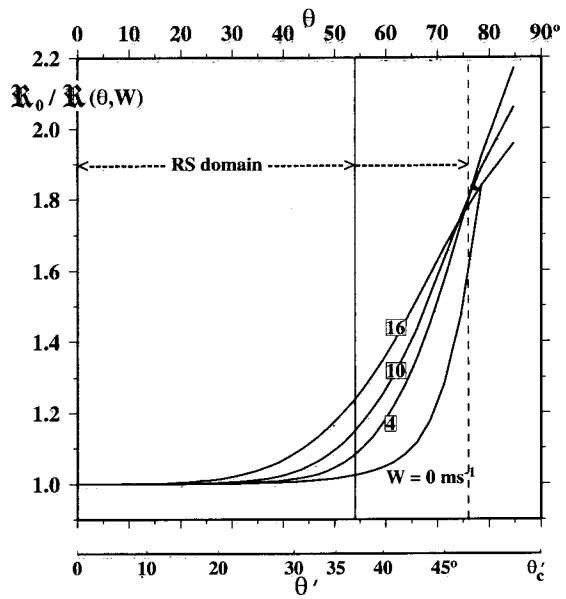

Fig. 4. Ratio $\Re_0/\Re(\theta, w)$ is plotted as a function of θ, for four wind speeds; θ_c' is the critical angle. The θ' scale in relation to the θ scale is also shown; the remote-sensing (RS) domain assumes that the maximal viewing angle (θ_v) is 47°, corresponding to $\theta \cong 54°$ ($\theta' \cong 37°$), for a satellite at an altitude of approximately 705 km, operating without tilt (solid vertical line). With a tilt of 20° [Sea-viewing Wide Field-of-view Sensor (SeaWiFS)], values as high as $\theta \cong 76°$ and $\theta' \cong 46°$ occur for the edges of the full swath (dashed line).

requirement. The underlying rationale was to produce from actual water-leaving radiances normalized quantities that are comparable. With this aim, the actual radiances (measured at sea or derived from satellite observation) must ideally be made independent from the illumination conditions at the instant of measurement. These conditions are essentially determined (at least for clear skies) by the Sun's position and the atmospheric diffuse transmittance. Therefore these environmental influences can tentatively be removed by forming the following quantity:

$$[L_w(\lambda)]_N = [L_w(0^+, \theta, \phi, \lambda)/E_d(0^+, \lambda)]F_0(\lambda), \quad (12)$$

where the measured radiance is divided by the actual irradiance at sea level, $E_d(0^+)$, and then multiplied by the solar irradiance at the top of the atmosphere, F_0, at the mean Sun–Earth distance (d_0). The above normalization can equally apply to field measurements (sea-truth validation) or to marine radiances derived from satellite data, after atmospheric correction.

The same $[L_w]_N$ quantity can be interpreted in another way: The normalized leaving radiance is the hypothetical radiance that would be measured if the Sun were at zenith, in the absence of atmosphere, and when the Earth is at its mean distance from the Sun. In spite of this interpretation (and in spite of its name), the normalized water-leaving radiance is still a quantity depending on geometry; indeed, the ocean is not a Lambertian reflector, and the initial quantity L_w [introduced in Eq. (12)] has been obtained under specific angular viewing conditions (θ, ϕ), when the Sun zenith angle (θ_s) was not zero, and thus has taken a particular value.

A way to remove this remaining dependence on the actual geometrical conditions consists of assuming that the observation was ideally made as though the pixel was seen vertically (nadir viewing) and the Sun was at zenith (such a hypothetical observation ignores the existence of the specular reflection of the Sun disk). This way is strictly in line with the initial approach developed by Gordon and Clark[29] and proceeds from the same logic.

Practically, it corresponds to carrying out the following operations: dividing $[L_w]_N$, obtained through Eq. (12), by the f/Q ratio that corresponds to the actual geometry and then remultiplying by the f/Q ratio corresponding to the hypothetical viewing situation ($\theta_s = \theta' = 0$). The same kind of operation must be repeated with respect to the factor $\Re$. When $\Re_0$ denotes the particular values of $\Re$ when $\theta' = 0$, f_0 denotes the particular f value when $\theta_s = 0$, and Q_0 denotes the Q value when θ_s *and* $\theta' = 0$, the above transformation is expressed through

$$[L_w]_N^{\text{ex}} = [L_w]_N \frac{\Re_0}{\Re(\theta', W)} \frac{f_0(\tau_a, W, \text{IOP})}{Q_0(\tau_a, W, \text{IOP})} \times \left(\frac{f(\theta_s, \tau_a, W, \text{IOP})}{Q(\theta_s, \theta', \phi, \tau_a, W, \text{IOP})} \right)^{-1}, \quad (13)$$

which produces the exact (superscript ex) normalized water-leaving radiance (see Appendix A of MG-96).

This operation requires the knowledge of all parameters involved ($\Re_0$, $\Re$, f_0, Q_0, f, and Q) for the various possible geometrical configurations, environmental conditions, and IOPs. From a practical viewpoint, look-up tables are a convenient solution. They are produced through radiative transfer computations that make use of a new bio-optical model for case 1 waters, combining the parameterizations proposed in Morel and Maritorena[11] and that of the phase function presented above. From this point, and because only case 1 waters are considered, the IOPs (as they appear in the above equations) are simply replaced by Chl, λ, inasmuch as these inherent properties are, for any wavelength, univocally expressed as a function of the Chl via an appropriate model.

C. Radiative Transfer Computations

The variations of the $\Re$ factor can be assessed through a specific Monte Carlo simulation, which involves only the wavy interface and combines Fresnel equations with the Gaussian distribution of capillary-wave slopes proposed by Cox and Munk.[30] The index of refraction of seawater is taken to be equal to 1.34 and spectrally constant. The results are shown (Fig. 4) in terms of the ratio $\Re_0/\Re(\theta', w)$, which is directly involved in Eq. (13). Tables are also available (see Appendix A).

The determination of the two other quantities, f and Q, requires that the in-water radiance field (particularly the upward field) be computed for all geometries, environmental conditions, and water types. This can be achieved by solution of the time-independent RTE for a coupled plane-parallel ocean–atmosphere system, including a wind-roughened interface. The invariant imbedding method, developed by Mobley[21] (and HYDROLIGHT 3.0 code), was generally employed, often in parallel with Monte Carlo simulations, to solve the RTE. An excellent agreement[8] between the radiance fields produced by the two methods was always obtained, including when Raman scattering was emulated. The atmospheric model originating from Gregg and Carder,[31] which was included in HYDROLIGHT, was used. The sky radiance field produced by this model does not appreciably differ from the one obtained with the more complex model previously used (as described in MG-96).

Only vertically homogeneous waters have been considered, and the case 1 water model used in MG-96 has been modified, not only for the phase function, which now depends on the Chl, as explained above, but also for the other IOPs. The spectral absorption coefficients of the water body, $a(\lambda, \text{Chl})$, are based on the recent statistical analysis (as a function of the Chl) of the diffuse attenuation for downward irradiance, $K_d(\lambda, \text{Chl})$. The $a(\lambda)$ values are derived from $K_d(\lambda)$ through an iterative procedure [Eqs. (8), (8′), and (8″) and Fig. 13 of Morel and Maritorena[11]]. Because K_d, which results from *in situ* measurements, cumulates the effects of all kinds of absorbing material present in the water column, the influence of yellow substance absorption is implicitly accounted for, at least on average. The (local or seasonal) changes that may occur in the Chl–yellow substance relationships are not reproduced in this empirical approach (it is likely that they are partly at the origin of the noise in the statistical K_d–Chl relationship[11]). The dependence of the particle scattering coefficient on the Chl has been recently reinvestigated, leading to the empirical relationship above [Eq. (8)] that is used here; the wavelength dependency of this coefficient is represented, as proposed in Ref. 11, through

$$b_p(\lambda, \text{Chl})/b_p(550, \text{Chl}) = (\lambda/550)^{v}, \qquad (14)$$

where the varying exponent v is expressed as

$$v = (1/2)[\log_{10}(\text{Chl}) - 0.3],$$

when $0.02 < \text{Chl} < 2$ mg m^{-3},

$$v = 0,$$

when Chl > 2 mg m^{-3}.

These expressions lead to featureless scattering spectra, flat or with an ascending slope toward the shorter wavelengths, depending on whether the Chl is above or below the threshold of 2 mg m^{-3}. The impact of absorption bands on the scattering spectra, detectable when the particle population is dominated by algal cells, is not represented when the above expressions are used.

The Raman-scattering coefficient (actually, the fractional absorption leading to reemission) is 2.6×10^{-4} m^{-1} at 488 nm, with a spectral dependency represented by λ^{-5} as in Bartlett *et al.*[32] Multispectral RTE computations (in the purely elastic mode and including the near-UV domain) are needed to encompass the whole excitation band corresponding to the emission at the wavelength of interest (see Mobley[21]). The spectral composition of the mean extraterrestrial solar radiation, $F_0(\lambda)$, is taken from Neckel and Labs.[33] For the results discussed below, the aerosol (maritime-type) optical thickness, τ_a (at 550 nm), was set equal to 0.2, and the wind speed was zero, which nevertheless leaves residual capillary waves (the constant term in Cox and Munk's formula[30]). The systematic computations have been carried out with the following entries:

- Wavelength, λ (seven values: 412.5, 442.5, 490, 510, 560, 620, 660 nm);
- Chlorophyll concentration, Chl (six values: 0.03, 0.1, 0.3, 1.0, 3.0, and 10 mg m^{-3});
- Zenith–Sun angle, θ_s (six values: 0°, 15°, 30°, 45°, 60°, and 75°);
- Azimuth difference, ϕ (13 values from 0° to 180°, increment of 15°);
- Nadir angle, θ' (17 values: 1.078°, 3.411°, 6.289°, 9.278°, 12.300°, 15.330°, 18.370°; 21.410°, 24.450°, 27.500°, 30.540°, 33.590°, 36.640°, 39.690°, 42.730°, 45.780°, and 48.830°).

With these increments, the total number of f values is 252 and that of Q values is 55,692; when restricted to the remote-sensing domain (i.e., with $\theta' \leq 36.64°$, $\theta < 53°$), the number of Q values reduces to 42,588 (see Appendix A for details and use of the tables).

3. Results

A. Physical Considerations

The varying nonisotropic character of the upward radiance field can be qualitatively explained from simple considerations (MG-93) summarized below. They involve two essential dimensionless parameters, namely, the single-scattering albedo, $\varpi = b/(a + b)$, from which one derives $\tilde{n}$, the average number of scattering events that the photons have undergone before reaching the interface and then forming the water-leaving radiance field:

$$\tilde{n} = (1 - \varpi)^{-1}, \qquad (15)$$

$$\eta_b = b_{bw}/(b_{bw} + b_{bp}), \qquad (16)$$

which is the ratio of molecular backscattering to the total (molecules and particles) backscattering coefficient.

When ϖ is small enough, single scattering prevails, so that the upward radiance field, at least within the Snell cone, is directly related to the shape of the VSF (centered on an axis that corresponds to the main

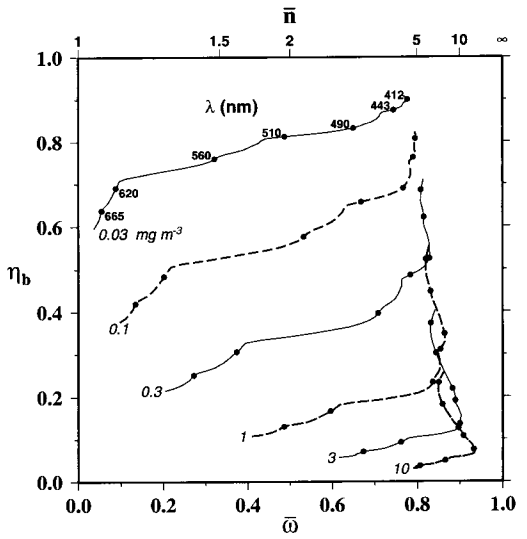

Fig. 5. Concomitant spectral variations of ϖ [or $\tilde{n}$, Eq. (15)] and η_b [Eq. (16)] for various Chls; reference wavelengths dealt with in the present study are indicated.

incident flux, i.e., the refracted direction of the Sun). According to the η_b value, the shape of the seawater VSF resembles that of molecular scattering when η_b is tending toward 1 or, conversely, that of the particle VSF (when η_b is small). Conversely, when ϖ, and thus $\tilde{n}$, increases, a multiple-scattering regime is set up; the upward field tends to become isotropic and less sensitive to the direction of the incident flux. The evolution toward a highly diffuse, quasi-isotropic, radiance field is rather slow and requires extremely large $\tilde{n}$ values[6] that are actually never reached in case 1 waters.

The above parameters $\varpi(\lambda, \text{Chl})$ and $\eta_b(\lambda, \text{Chl})$, computed on the basis of the renewed IOPs parameterization, are displayed in Fig. 5 (a revised version of Fig. 6 of MG-93). Note that in case 1 waters, the highest $\tilde{n}$ value is approximately 15 when Chl = 10 mg m^{-3} (at λ = 560 nm), whereas the lowest ones are always in the red part of the spectrum. Molecular backscattering dominates in low-chlorophyll waters ($\leq$0.1 mg m^{-3}).

B. Variations of the *f* Factor

The impacts on the *f* values subsequent to the new parameterization of case 1 water IOPs are globally shown in two steps on Figs. 6(a) and 6(b). The first one compares the new results, computed in the purely elastic mode, to those of MG-96. On average, the new *f* values are above the previous ones by approximately 10%–20%, and the largest differences are for the highest Chl values and a large Sun zenith angle. In the second step the new results, including the inelastic Raman scattering, are compared with the results obtained in the purely elastic mode. There are only minute differences between the two sets of numerical data, except for the "cloud" that contains exclusively the lowest Chl values (<0.3 mg m^{-3}) and radiations (620 and 660 nm) in the red domain. Because the Raman emission adds a flux to the elastically backscattered flux, this process directly affects, i.e., raises, all the *f* values for all wavelengths (regardless of the Sun's position). This impact is maximal when the elastic scattering is minimal, namely, for waters with low Chl and low particle content. In such a case, for instance, when Chl = 0.03 mg m^{-3}, the increase in *f* is more important (+15%) in the red part of the spectrum (660 nm), in which the scattering coefficient (because of water and particles) is low, than it is in the blue part (+5%, at 442.5 nm), in which the ($\lambda^{-4.3}$) molecular scattering limits the decrease in the scattering coefficient. The Raman emission has no significant effect on the *f* factor when the elastic scattering becomes important, as it is in the case when the Chl is, say, above 1 (or even 0.3) mg m^{-3}.

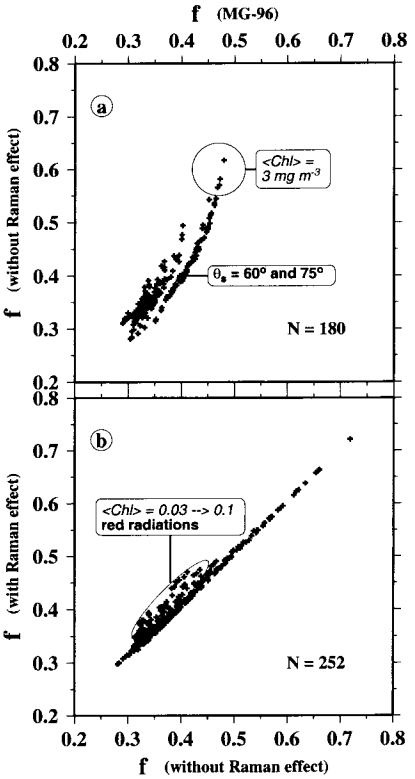

Fig. 6. (a) Comparison of the new *f* values, when the Raman emission is not included, with the previous ones (MG-96); the Chl is limited to 3 mg m^{-3}. (b) New *f* values, computed with or without Raman inelastic scattering (the Chl is as high as 10 mg m^{-3}).

Even though the *f* values have changed as a result of the present computations, the general behavior remains unmodified. The causes of their variations were analyzed in MG-91, MG-93, and MG-96, and these previous analyses remain valid. These variations can be described and summarized as follows:

- Whatever the wavelength and the Chl, *f* is minimal when θ_s is 0; i.e., when *f* is f_0;

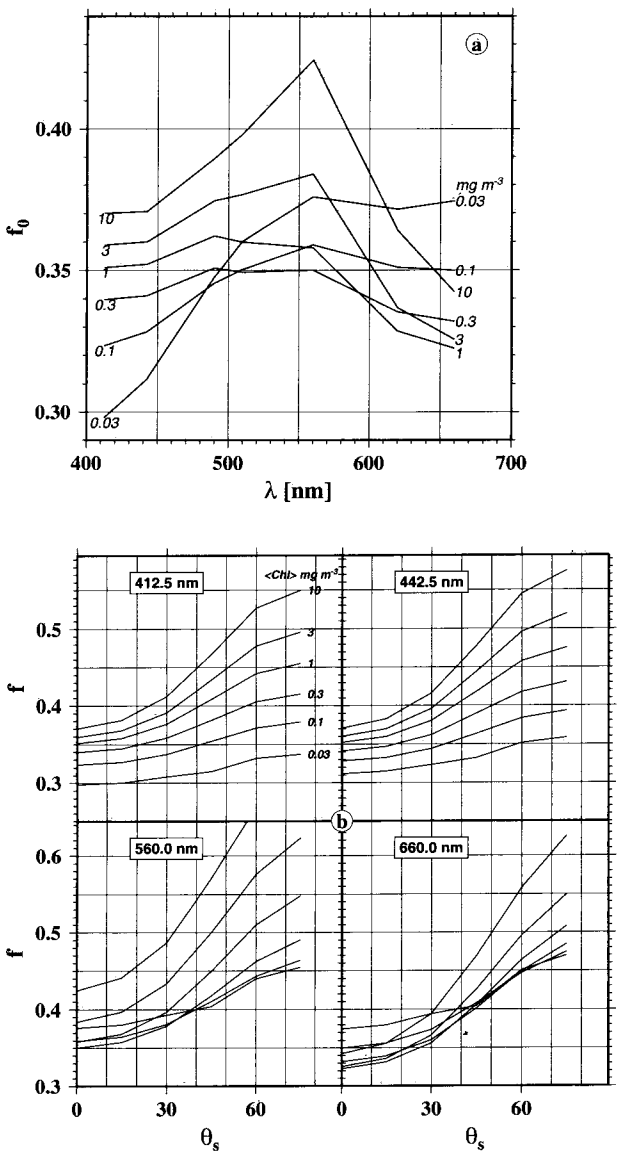

Fig. 7. (a) Spectral values of the factor f_0 for various Chls, as indicated. (b) Evolution of the f factor with the solar zenith angle, for six Chl values and four selected wavelengths, as indicated.

- The spectral dependency of f_0 is weak in the middle of the Chl range and pronounced for the extreme values, 0.03 and 10 mg m^{-3} [Fig. 7(a)];
- f monotonously increases when θ_s increases to $\theta_s = 75°$ [Fig. 7(b)]; actually, it is linearly related to cos θ_s in the domain 0° to 60° (Appendix B);
- For a given θ_s and at a fixed wavelength, f is always increasing with the Chl;
- The sun-dependent variations in f are increasingly wider for increasing Chl.

These last two points regarding the f(Chl, θ_s) values and variations are directly related to the η_b value (MG-91); lower f values and a lesser dependence on θ_s are expected when η_b is increasingly high. Thus the results in Fig. 7(b) can be understood from the η_b patterns shown in Fig. 5.

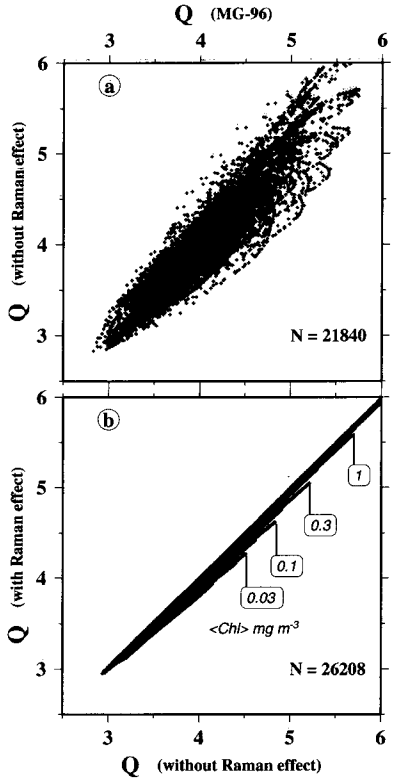

Fig. 8. (a) Comparison of the new values of the bidirectional function Q, when the Raman emission is not included, with the previous ones (MG-96); the Chl is limited to 3 mg m^{-3}. (b) New Q values, computed with and without Raman inelastic scattering (the Chl is as high as 10 mg m^{-3}). The departures (lowering of the Q values) resulting from the Raman influence when the Chl is low enough are identified.

C. Variations of the Bidirectional Function, Q (θ_s, θ', ϕ, λ, Chl)

As for f, the comparison of the present computations with those in MG-96 is performed in two steps. In Fig. 8(a), in which the Raman effect is not considered, it can be seen that there is no systematic difference between the two sets of Q values (the regression analysis provides a 1.01 slope) in spite of an important scatter; individual differences are notable and may reach approximately ±15% at the most (for the highest θ_s and Chl values). The identification of the points in this graph does not provide a clear indication of the way the differences are organized (with respect to Chl, λ, θ_s, θ', and ϕ). The respective roles of the five parameters in the scatter of the points in Fig. 8(a) are interwoven in a complex fashion. The only distinguishable trend would be with respect to the Chl; when the Chl is low, the new Q values are lower than the previous ones, and, conversely, higher Q values are obtained for Chl $\geq$ 3 mg m^{-3}. This means that the present Q values, compared with the previous ones, encompass a slightly wider range.

The consideration of the Raman emission does not entail a drastic change in Q [Fig. 8(b)]. The depressive effect on Q (by a few percents only) is regularly organized; i.e., it increases with decreasing Chl.

The Raman emission, which is characterized by a phase function nearly isotropic (similar to the molecular scattering phase function), has therefore a weak influence on the bidirectional Q function. Indeed, at low Chl, the Raman emission is not negligible and adds to the elastic backscattering. This backscattering, which is predominantly due to molecules, is already characterized by a quasi-isotropic angular distribution, and thus the general angular pattern is not notably modified. At moderate and high Chls, the elastic scattering becomes more featured (owing to particle scattering), and the effect of the Raman emission is a smoothing of the radiance angular pattern; the elastic particle scattering, however, is predominant and drowns the Raman emission.

As for f, the differences observed [Fig. 8(a)] do not affect the general behavior of the Q function, already examined in MG-96 (their Figs. 3 and 4); they are briefly recalled and illustrated by Figs. 9(a) and (b).

- As a first observation, the particular Q value, denoted Q_0 (when $\theta = \theta' = 0$), is almost spectrally flat and regularly increasing with the Chl, from approximately 3.1 to 4.4 [Fig. 9(a)].
- The particular Q value, denoted Q_n, corresponding to a radiance originating from nadir ($\theta' = 0$), is an increasing function of both the solar zenith angle and the Chl [Figs. 9(b) and 9(c)]; this holds true for all wavelengths. Actually, Q_n is linearly related to $\cos\theta_s$ in the domain $0° < \theta_s < 60°$ (see Appendix B).
- The angular pattern of the Q function with θ' can be visualized within the solar principal plane by use of a polar diagram as in MG-93 (their Fig. 2). The minimal and maximal Q values are found in this plane. Some contrasted examples, with extreme values in terms of the Chl and λ, are displayed in Fig. 10. They practically encompass the whole range of variations to be expected in case 1 waters. The radiance patterns are either influenced by the shape of the molecular backscattering function (high η_b) or by that of particles (low η_b); increasing $\tilde{n}$ tends to smooth the pattern (by multiple scattering) even if an isotropic regime is far from being attained, even when $\tilde{n} = 15$.

D. Variations of the *f*-to-*Q* Ratio

In reference to Eq. (13), the particular quantity f_0/Q_0 will be examined first, as a function of the wavelength and for varying Chls (Fig. 11). The overall range of variation of this quantity is $0.08 - 0.12\ \mathrm{sr}^{-1}$. The extreme values occur in the red part of the spectrum because the Raman scattering is considerable at low Chl ($<1\ \mathrm{mg\ m}^{-3}$) and results in increases in f_0. In the blue part the variations remain within a narrower interval, whatever the Chl (between 0.086 and 0.097).

The examination of Figs. 7(b) and 9(b) shows that both quantities f and Q_n experience concomitant increases when the sun zenith angle increases. Therefore their ratio, and, in general, any f-to-Q ratio, is less dependent on θ_s than f and Q separately considered. The strongest angular variations in f/Q (with respect to θ') are expected to occur within the principal plane, whereas they are minimal in the perpendicular plane ($\phi = \pi/2$). Typical values of this ratio (Fig. 12) are in the range of 0.08–0.15 (around the mean value 0.11, as found by Gordon *et al.*[12]). When approaching the critical angle ($\approx 48°$), higher f/Q values are possible, particularly for a large sun zenith angle and high chlorophyll.

The spectral dependency of the f/Q ratio is marked for low Chl ($\mathrm{Chl} = 0.03\ \mathrm{mg\ m}^{-3}$) essentially because the influence of the Raman scattering is important for the green and red radiations. When the Chl is in the range of 0.3–1 $\mathrm{mg\ m}^{-3}$, the spectral dependency of f/Q has practically vanished; it reappears at 3 $\mathrm{mg\ m}^{-3}$. Strongly featured f/Q angular patterns at all wavelengths are typical of high concentrations. It must be noted that the asymmetrical f/Q pattern (when the solar angle departs from 0°) is reversed from low to high Chls.

4. Discussion and Conclusions

A. Importance of the Bidirectional Correction in the Frame of Remote Sensing

Independently of the efficiency of the atmospheric correction process, and therefore independent of the accuracy in the ocean color signal retrieval (not discussed here), it is important to quantify the magnitude of the bidirectional corrections, by which the normalized water-leaving radiance can be transformed into an exact one [Eq. (13)]. The critical ratios for this transformation, namely, $\Re_0/\Re$, f_0/f, and Q/Q_0, are successively examined below.

The first ratio (already displayed in Fig. 4) remains practically equal to 1 for directions corresponding to the center of the swath of a remote sensor. The correction, always by a factor >1, becomes notable for slant directions (toward the edges of the swath) and is increasingly important when the wind speed (W) increases. There is a limitation in the predictions at high wind speed, in particular because the fractional area of the surface covered by white caps increases (approximately 2% for $W = 16\ \mathrm{ms}^{-1}$), so that another type of correction is also needed (not discussed here).

The second ratio, f_0/f, is always below 1 (Fig. 13). When θ_s increases (from 0° to 75°), f_0/f systematically decreases, from 1 to approximately 0.8–0.9 when $\mathrm{Chl} = 0.03\ \mathrm{mg\ m}^{-3}$ or approximately 0.55–0.65 when $\mathrm{Chl} = 10\ \mathrm{mg\ m}^{-3}$; the largest corrections always correspond to the largest solar zenith angles and Chl. Conversely, the third ratio, Q/Q_0, (Fig. 14) lies mostly (but not always) above 1; again, the widest variations are observed for high Chl.

Finally, the combination of the three ratios—namely, $(f_0/f)\ (Q/Q_0)(\Re_0/\Re)$—as it appears in Eq. (13), is illustrated by Figs. 15(a) and 15(b). The various trends separately exhibited by the three ratios (f_0/f systematically <1, Q/Q_0 generally >1, and $\Re_0/\Re > 1$) scarcely compensate. For $\mathrm{Chl} > 1\ \mathrm{mg\ m}^{-3}$, the combination of the three ratios is systematically below 1. This means that the exact normalized water-leaving radiance, $[L_w]_N^{\mathrm{ex}}$, will be, in

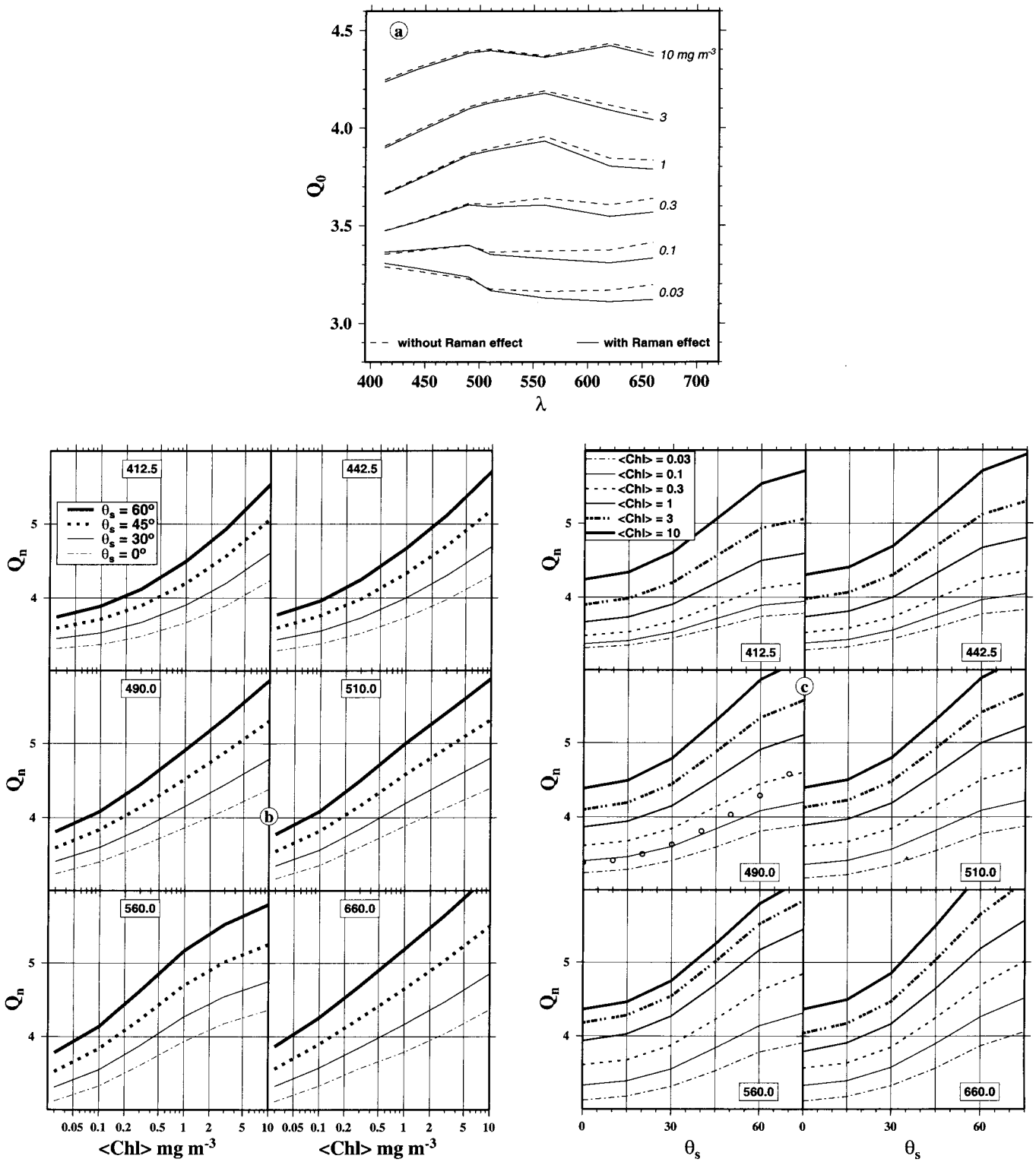

Fig. 9. (a) Spectral values of the Q_0 function computed with and without the Raman emission for six Chl values, as indicated. (b) Evolution of the Q_n function with increasing Chls for various wavelengths and solar zenith angles, as indicated. (c) Q_n as a function of the solar zenith angle for various wavelengths and Chls [same data as in (b)]; the open symbols correspond to Eq. (17).

general, smaller than the uncorrected one $[L_w]_N$. The difference resulting from the correction may be as high as −50% in exceptional circumstances (Chl = 3 or 10 mg m^{-3}, large θ_s, large θ', and, in the red part of the spectrum, $\lambda \geq 560$ nm). At low Chl (<0.1 mg m^{-3}), the differences are less and in both directions (by a factor >1 or <1). At intermediate concentration (e.g., 0.3 mg m^{-3}), $[L_w]_N^{ex}$ and $[L_w]_N$ are gen-

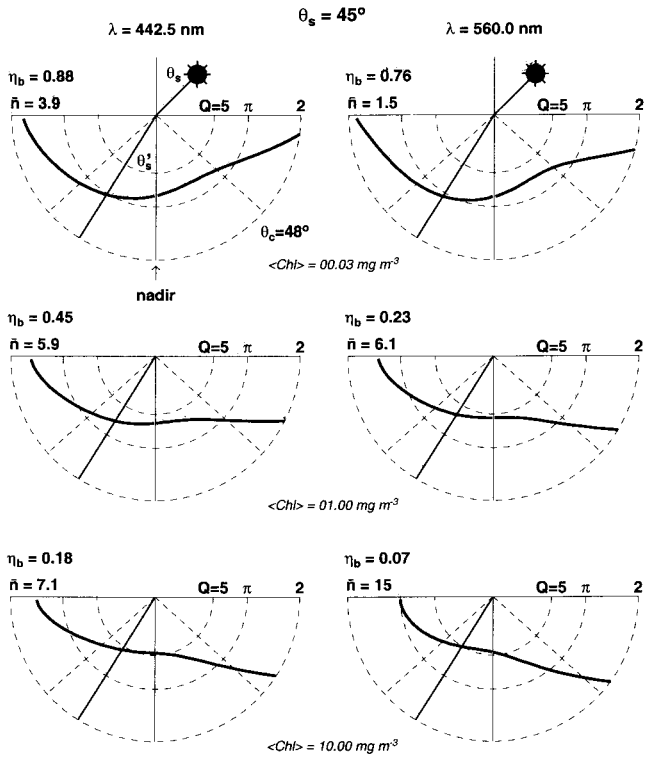

Fig. 10. Polar representation in the solar principal plane of the upward radiance field, normalized by the upward irradiance [i.e., the ratio $L_u/E_u = Q^{-1}$, Eq. (10)] for three Chl values (rows) and two wavelengths (columns). This polar diagram represents the normalized radiances as vectors, the length of which corresponds to magnitude, ending at the center. The solar zenith angle is 45° in air (31.8° in water), and the $\bar{n}$ and η_b values for each case are indicated, as well as the critical angle (48°).

erally closer, and the maximal difference (approximately −20%) occurs for large θ_s. The influence of the wind speed (through $\Re_0/\Re$) is also shown (open circles in Fig. 15). Examples of applying such corrections will be given below.

B. Observation of the Bidirectional Effects

The radiance distribution determined in Lake Pend Oreille, Idaho, by Tyler[35] (see also Tyler and Preisendorfer[36]) and the radiance fields for various sun angles measured by Voss[4] in case 1 waters (west of San Diego) encompass the whole upward half-space and thus form the most complete set of accurate radiance determinations. The Q values from the previous tables were successfully tested[5] against these data. The same test repeated with the present tables does not show palpable differences (a few percents at the most), which is not surprising. Indeed, the new and previous Q tables are almost coinciding for the IOPs of the Lake Pend Oreille or for those of Californian waters (in which the Chl value was close to 0.3 mg m^{-3}).

The dependence of Q_n (at 5-m depth) on the sun angle has been established for blue light (465–474 nm) in Mediterranean waters by Aas and Hojerslev[37]; according to these authors, the observed variations

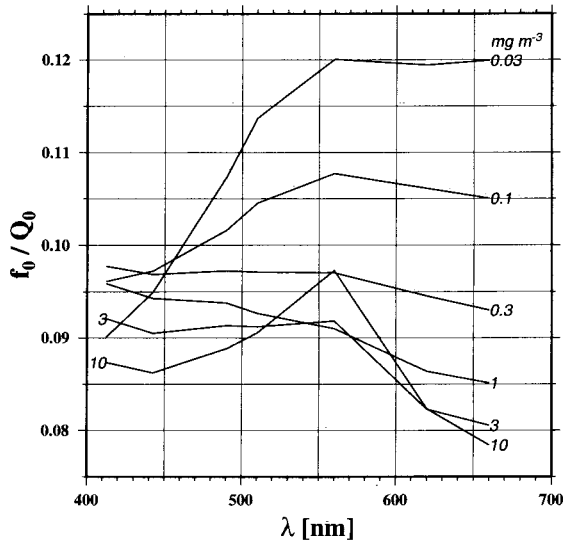

Fig. 11. Spectral values of the f_0/Q_0 ratio for the six Chls, as indicated.

are approximately described by the empirical relationship

$$Q_n = (5.20 \pm 0.24) - (1.82 \pm 0.035)\cos\theta_s. \quad (17)$$

The theoretical predictions made for 490 nm and a Chl of 0.1 mg m^{-3} (as estimated for these waters) agree well with the values derived from the above expression for the angular domain 0°–45° [Fig. 9(c)], whereas a slight divergence occurs for larger Sun zenith angles. In the same field study, the upward radiance field (at 5 m) was also determined in the principal plane for different Sun positions. These data (Fig. 4 of Ref. 36) and the theoretical predictions (Chl = 0.1 mg m^{-3}; 465 nm) are comparatively displayed in Fig. 16. There is an overall agreement regarding the distribution of the data and the shape and respective position of the computed curves. Trials with other Chls (0.05 and 0.2 mg m^{-3}) do not return a better fit. The high radiance values recorded in the horizontal direction (particularly toward the Sun) disagree with theoretical predictions. For these data, the environmental conditions and instrumental limitations are not known with enough accuracy to allow this satisfactory comparison to be more than a qualitative one.

The three-year time-series measurements made near Venice, in Adriatic coastal waters,[38] show on average an increase in Q_n with increasing Sun zenith angle; yet the changing optical properties, chlorophyll content, and even water types (from case 1 to case 2 waters) in this location preclude going beyond a rough confirmation of the theoretical trends.

The bidirectional effects are clearly shown in ocean color imagery. An example is provided in Fig. 17. A rectangular zone (delimited by the 35–33 °N parallels and the meridians 18–28 °E) located in the oligotrophic eastern Mediterranean Sea (Chl < 0.1 mg m^{-3}) has been selected because of a reduced cloud cover and a relative homogeneity of the optical prop-

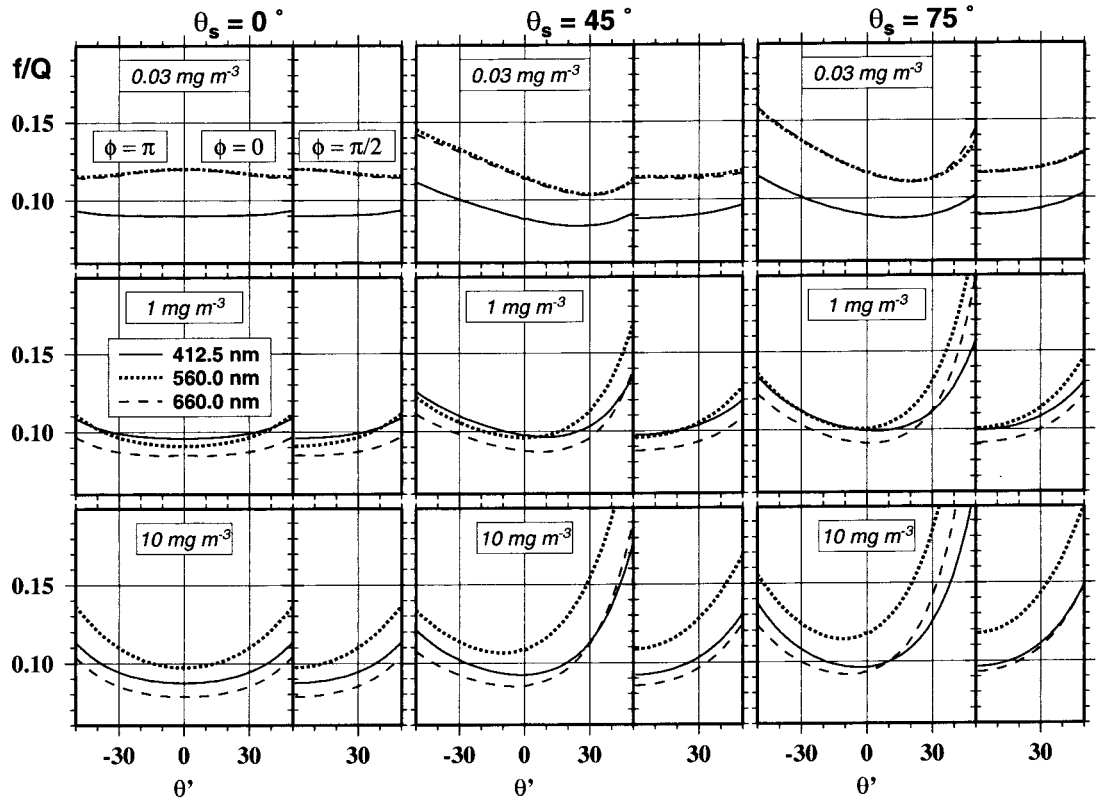

Fig. 12. Selected examples of the f/Q ratio as a function of θ' (restricted to $\pm 50°$) within the principal plane ($\phi = 0$ or π) and within the perpendicular half-plane ($\phi = \pi/2$). This figure is to be compared with Fig. 6 of MG-96 (a similar figure for other Chls is also provided in Ref. 34).

erties and also because observations at sea were made in 1999, during a five-day station in the center of this zone (34 °N, 22 °E, day-of-the-year # 263 to 267), and in its vicinity (days 262 and 269). The observed wind speed was between 3 and 6 m s^{-1}. The Sea-viewing Wide Field-of-view Sensor[39] (SeaWiFS) normalized water-leaving radiances [Eq. (12)] within this zone were computed from local area coverage data for days 258, 262, 263, 264, and 269 by use of the SeaWiFS Data Analysis System (version 4).

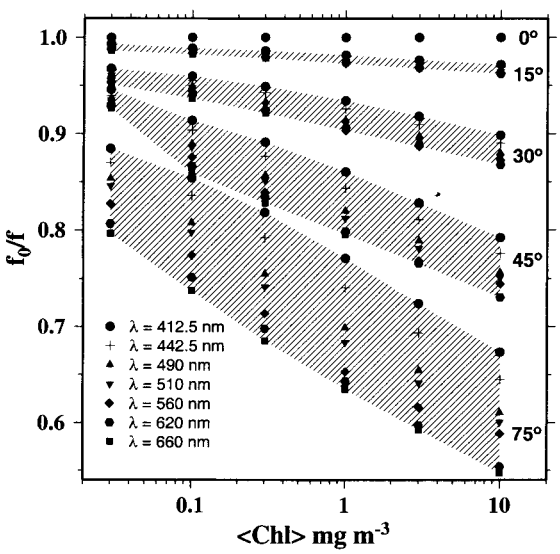

Fig. 13. Evolution of the f_0/f ratio with the Chl and for solar angles as indicated by the shaded areas (the values for $\theta_s = 60°$, which overlap those for 45° and 75°, are not displayed); the symbols are for the various wavelengths.

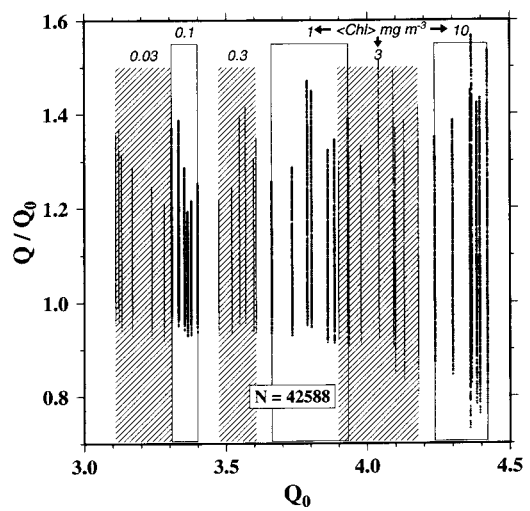

Fig. 14. Variations in the Q/Q_0 ratio. The horizontal scale is based on the Q_0 (Chl, λ) values, which allow the various Chl domains to be discriminated (shaded or white vertical bands). Each band contains six vertical lines corresponding to the six wavelengths (not indicated); each vertical line corresponds to an accumulation of dots displaying the Q/Q_0 values, for all θ_s, ϕ, and θ' values.

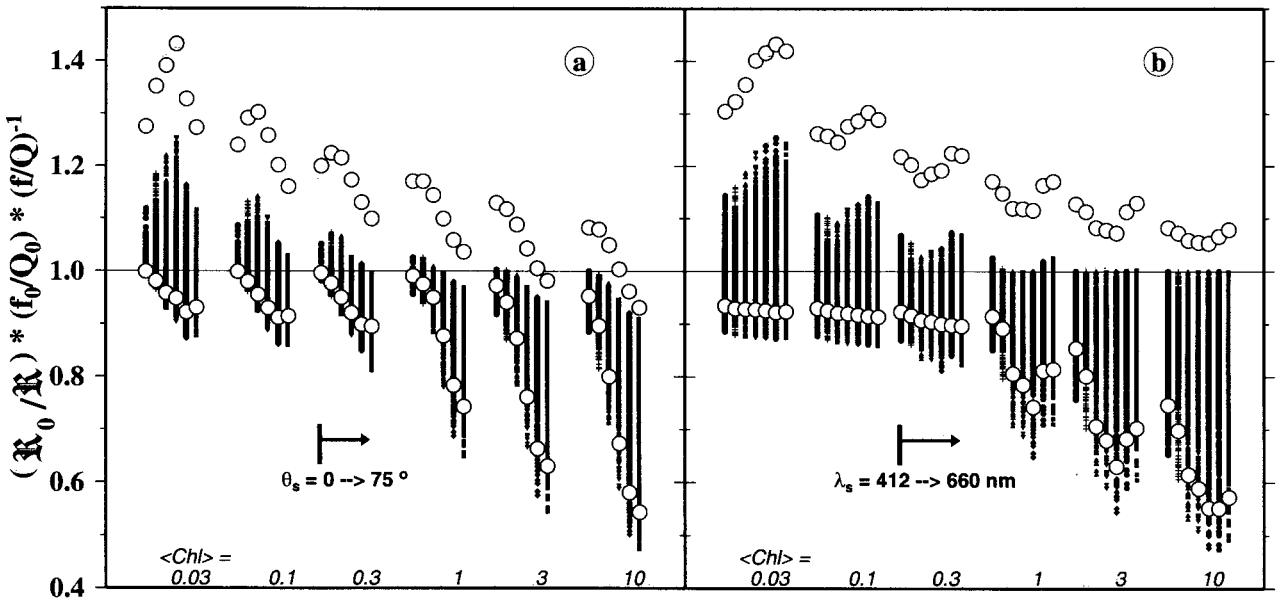

Fig. 15. Variations in the $(\Re_0/\Re)(f_0/Q_0)(f/Q)^{-1}$ quantity [the corrective term appearing in Eq. (13)], plotted as a function of the Chl. (a) The vertical bars are made of the dots corresponding to all ϕ and λ values and to the θ' values less than 37° (cf. Fig. 4); The six vertical bars in each grouping correspond to the six solar angles (θ_s = 0°, 15°, 30°, 45°, 60°, and 75°), whatever λ. (*b*) As in (*a*) except for the grouping that now corresponds to the discrete wavelengths (412.5, 442.5, 490, 510, 560, 620, 660 nm), whatever θ_s. The $(\Re_0/\Re)$ values used for this figure are those computed for a wind speed of 4 m s^{-1}. With increasing speed, all the vertical bars migrate slightly upward; especially the upper values (which always correspond to large θ') are significantly enhanced. The corresponding lower and upper ends of the bars for W = 16 m s^{-1} are shown as open circles.

They have been averaged (to reduce the noise) along the north–south direction (over a zonal band spanning 2° in latitude), so that only a single mean longitudinal radiance profile is produced from each scene and day. These profiles, however, correspond to differing geometrical configurations regarding the Sun's position and viewing angles. In effect, the selected zone is sometimes seen in the middle of the swath and sometimes near the western edge (once) or the eastern edge (twice) of the swath. Note that the extreme pixels near the very edges (scan angle > 52°, approximately) were never used when the zonal average was computed because of high noise and devi-

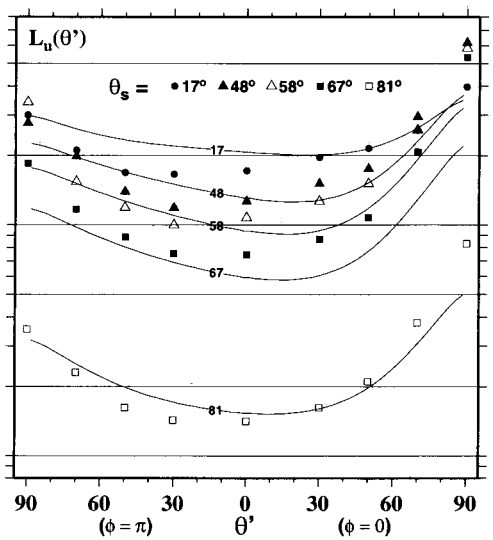

Fig. 16. Upward radiance field $L_u(\theta')$ (arbitrary units) at a depth of 5 m and λ = 465 nm for various Sun zenith angles θ_s. The symbols are reproduced from Fig. 4 of Ref. 36 and represent data obtained in the Mediterranean Sea (south of Sardinia, 2 July 1971). The curves have been computed for the same θ_s and with Chl = 0.1 mg m^{-3}. The vertical log scale (arbitrary units) allows the two kinds of result to be put in approximate coincidence by translation, without changing the respective positions of either the theoretical curves or the experimental data.

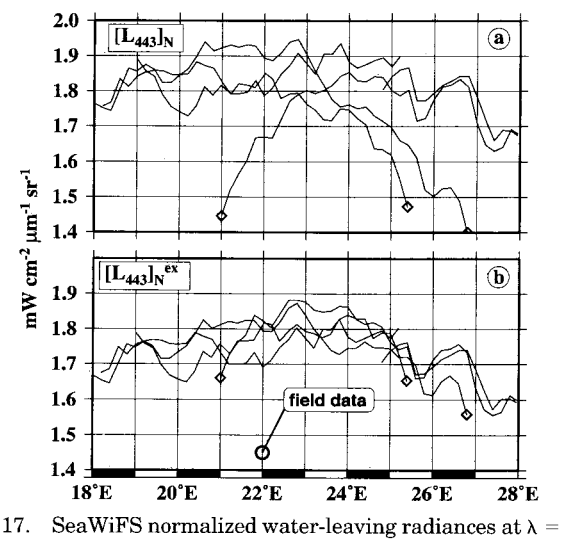

Fig. 17. SeaWiFS normalized water-leaving radiances at λ = 443 nm, (a) before and (b) after bidirectional corrections (see text). The circle represents the average value derived from field reflectance measurements (at 22 °E, 34 °N) carried out during the same period. The Chl in this zone is below 0.1 mg m^{-3}. The diamonds show the extreme pixels considered near the swath edge, before and after correction.

ant values. The changing geometry results in perturbations within the profiles. In particular, noticeable drops in the normalized radiances are observed for pixels at the edges of the swath (eastward or westward). If the radiances are converted into exact normalized water-leaving radiances [by use of Eq. (13), the f/Q tables, and the $\Re_0/\Re$ table with $W = 4\ \mathrm{m\ s^{-1}}$] before the average profiles are computed, these anomalies disappear, and the profiles are smoother and become coincident. The exact water-leaving radiances [1.75 mW $\mathrm{cm^{-2}}$ $\mu\mathrm{m^{-1}}$ $\mathrm{sr^{-1}}$] are on average lower (by approximately 5%) than the uncorrected values. They, however, remain above those derived from field measurements made during the cruise of the Productivité des Systèmes Océaniques Pélagiques[40] (PROSOPE) (Productivity of Pelagic Oceanic Systems). Indeed, at 22 °E, the irradiance reflectance at 443 nm was steadily around 4.8% (14 measurements over five days), which would lead to $[L_w]_N^{ex} \approx 1.45$ mW $\mathrm{cm^{-2}}$ $\mu\mathrm{m^{-1}}$ $\mathrm{sr^{-1}}$. This discrepancy, likely originating from an imperfect atmospheric correction, is out of the scope of the present discussion.

C. Final Remarks

With respect to the studies of the bidirectional reflectance in MG-91, MG-93, and MG-96, the present paper has incorporated three major modifications. First, the inelastic Raman scattering has been considered in addition to the elastic scattering by molecules and particles. Second, the parameterization of the IOPs in case 1 waters (absorption, total scattering, and backscattering) as a function of the Chl has been modified according to the results of recent reexaminations.[11,28] Finally, and in a more realistic fashion, the shape of the particle phase function has been made a function of the Chl. Therefore this function becomes consistent with the backscattering parameterization proposed in Ref. 13. It is clear, however, that if the earlier inconsistency (resulting from the use of the Petzold function, which forced the backscattering probability to be independent from the Chl) is removed, it is replaced by assumptions regarding the phase function for small and large particles and the mixing law. These assumptions, believed to be reasonable, remain to be verified by detailed measurements not yet available.

As a result, the present tables containing the essential bidirectional parameters f and Q (and their ratio) are believed to be superior and more realistic than the previous ones. In particular, the weaknesses, which have been previously identified and regularly acknowledged in the case of waters with moderate to high Chls is, in principle, removed. For waters with low Chl, and thus low elastic particle scattering combined with a low molecular scattering in the red part of the spectrum, a definite improvement comes from the inclusion of the Raman emission, which was ignored in the previous calculations. The new tabulated values, however, do not dramatically differ from the previous ones [Figs. 6(a) and 8(a)] and reveal the same general behavior, which is somewhat comforting for another reason, as explained below.

Indeed, it cannot be claimed that the parameterizations offered in this paper are the last words to describe the optical properties of case 1 waters; were they (on average) rather well parameterized with respect to the Chl, these bio-optical properties are anyway expected to vary (spatially and temporally) as a consequence of the natural variability within the relationships and proportions between the Chl and the other optically active components. Therefore the absence of marked discrepancies between the previous and present tables (a kind of sensitivity test with respect to several input parameters globally considered) indicates that the main trends are already captured, so that correcting for the bidirectional effect can presumably be made in a rather safe manner by use of the present tables. Sensitivity tests based on the known variability[28] of some input parameters separately considered [e.g., b_p in Eq. (8)] or on an assumed variability in the backscattering properties [e.g., Petzold's value versus Eq. (1)] lead to the same conclusion.

As presently the RTE can be accurately solved,[8] future improvements in the knowledge and prediction of the bidirectional effects are not to be expected from computations themselves. They can result only from a reinforcement of experimental efforts. Systematic measurements focused on input parameters, especially the particle VSF, its backward lobe, and its spectral dependency for varying phytoplankton concentration, are needed. Measurements are also necessary for the validation of the outputs, through the determination of in-water radiance fields at various wavelengths for differing solar elevation, and in well-controlled conditions, with respect to the IOPs.

Appendix A

The results of computations are available over the Internet, by use of anonymous ftp, from oceane.obs-vlfr.fr, then cd pub/gentili/AppliedOptics2002. The main characteristics of these tables are summarized below.

The quantities $f(\lambda, \theta_s, \mathrm{Chl})$ and the ratios $f(\lambda, \theta_s, \mathrm{Chl})/Q(\lambda, \theta_s, \theta', \phi, \mathrm{Chl})$ are tabulated as functions of the five following parameters:

- Wavelength (λ), seven values;
- Zenith-sun angle (θ_s), six values;
- Chlorophyll concentration (Chl), six values;
- There are 252 ($6 \times 6 \times 7$) separate files. Each file contains 13 columns and 17 lines; the columns are for 13 azimuth differences (ϕ), and the lines are for the nadir angles (17 θ' values). Note that the value for the first nadir angle (1.078°) is to be used for $\theta' = 0$.

There are two sets of tables in the same format, one is for computations with the Raman effect included, and one is for computations without this effect. The first one is to be used for bidirectional corrections,

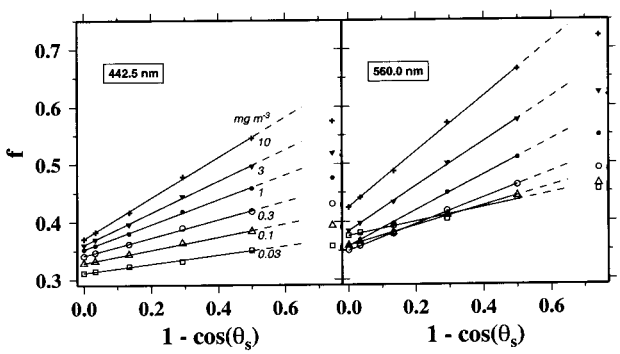

Fig. 18. Selected examples of the computed f factor plotted as a function of $(1 - \cos \theta_s)$ and the corresponding linear fit valid within the interval $0 < \theta_s < 60°$ [Eq. (B1) and Table 1].

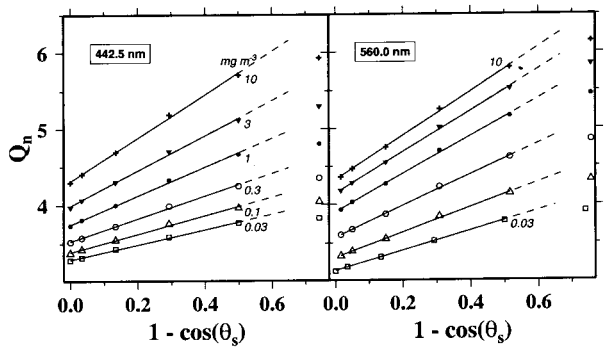

Fig. 19. Selected examples of computed Q_n values plotted as a function of $(1 - \cos \theta_s)$ and corresponding linear fits valid within the interval $0 < \theta_s < 60°$ [Eq. (B2) and Table 2].

whereas the second one is provided essentially for comparison with results obtained through modeling studies that cannot account for transspectral effects.

A separate table provides the quantity $\Re(\theta', W)$ at a θ' increment of 1°, for a perfectly level interface, and for wind speeds $W = 0$, 4, 10, and 16 m s^{-1}. Residual capillary waves still exist when $W = 0$, so that the $\Re(\theta', 0)$ values slightly differ from those computed when the interface is assumed to be perfectly flat.

Appendix B

The factor f [Fig. 7(b)] increases with θ_s in a rather regular manner, as long as $\theta_s < 60°$; actually, within this domain, f is linearly related to $\cos \theta_s$ (when $\cos \theta_s > 0.5$), according to relationships such as (see examples in Fig. 18)

$$f(\theta_s, \lambda, \text{Chl}) = f_0(0, \lambda, \text{Chl}) + S_f(\lambda, \text{Chl})(1 - \cos \theta_s). \quad \text{(B1)}$$

The departure from linearity is less than 0.5% when $\theta_s < 45°$ and may reach 2% in some cases (when $\theta_s = 60°$). Attempts to parameterize f_0 and S_f as a function of both λ and Chl lead to complicated, and in the end less accurate, polynomials. Therefore it is more convenient to present f_0 and S_f under tabulated forms (Table 1 below).

The same analysis can be repeated for the parameter Q_n [Fig. 9(c)]. According to Fig. 19, the fit-to-linear equations involving again $(1 - \cos \theta_s)$ is excellent if $\theta_s < 60°$; the relative error always remains below 1%. Accordingly, Q_n can be expressed as

$$Q_n(\theta_s, \lambda, \text{Chl}) = Q_0(0, \lambda, \text{Chl}) + S_{Q_n}(\lambda, \text{Chl})(1 - \cos \theta_s), \quad \text{(B2)}$$

and the needed parameters are to be found in Table 2.

These simple expressions are useful when calibration–validation measurements are performed at sea by use of the in-water method. According to the protocols,[34] the upward radiance, measured under water (by aiming at nadir, $\theta' = 0$), is then propagated through the interface to provide $L_w(0^+)$. Simultaneously, the downwelling irradiance $E_d(0^+)$ is measured above the surface, so that Eq. (12) can be operated to obtain $[L_w]_N$. As these measurements are generally carried out when the Sun zenith angle differs from 0, the transformation described by Eq. (13) is necessary to produce the exact normalized

Table 1. f_0 Parameter and the Associated Slope of Its Relationship to the Cosine of the Sun Zenith Angle

Parameter	Wavelength (nm)						
f_0 (mg m^{-3})	412.5	442.5	490	510	560	620	660
0.03	0.297892	0.311742	0.347280	0.359728	0.375008	0.370053	0.372716
0.1	0.324018	0.328848	0.345755	0.350503	0.358735	0.350497	0.349206
0.3	0.340239	0.341657	0.350980	0.349334	0.349570	0.334437	0.330755
1	0.351673	0.352505	0.362207	0.359773	0.357388	0.327275	0.320913
3	0.359587	0.360429	0.374357	0.376513	0.383433	0.335178	0.323731
10	0.370570	0.370782	0.389128	0.397841	0.424316	0.362306	0.340204
S_f (mg m^{-3})							
0.03	0.065801	0.076526	0.095435	0.103901	0.121165	0.134426	0.143912
0.1	0.095786	0.111534	0.138252	0.147280	0.169210	0.183429	0.195362
0.3	0.131988	0.154209	0.191203	0.201694	0.225606	0.227381	0.236441
1	0.183170	0.213187	0.261757	0.276009	0.305781	0.284162	0.285455
3	0.239626	0.273898	0.330935	0.349059	0.386471	0.352961	0.343078
10	0.316124	0.351720	0.415626	0.438584	0.482277	0.457638	0.433943

Table 2. Q_0 Parameter and the Associated Slope of Its Relationship to the Cosine of the Sun Zenith Angle

Parameter	Wavelength (nm)						
Q_0 (mg m^{-3})	412.5	442.5	490	510	560	620	660
0.03	3.318220	3.291250	3.245640	3.176500	3.138020	3.116680	3.126530
0.1	3.375400	3.385700	3.408430	3.359680	3.336890	3.309970	3.332380
0.3	3.484950	3.529680	3.613410	3.601660	3.606950	3.542300	3.560200
1	3.675060	3.746830	3.868930	3.894090	3.942030	3.815240	3.801910
3	3.913530	3.991380	4.110030	4.141140	4.188650	4.104160	4.053610
10	4.252700	4.313260	4.393950	4.405460	4.368130	4.427190	4.371050
S_{Q_n} (mg m^{-3})							
0.03	0.863223	0.976278	1.129290	1.203100	1.296770	1.413010	1.479420
0.1	1.055510	1.190090	1.382130	1.482910	1.625960	1.775070	1.866290
0.3	1.302830	1.469930	1.700680	1.827460	2.036100	2.175700	2.269360
1	1.671180	1.877700	2.115910	2.239960	2.479820	2.711180	2.789710
3	2.083950	2.303690	2.506640	2.580090	2.707700	3.141310	3.229040
10	2.625950	2.843750	2.978790	2.986960	2.898750	3.527960	3.717540

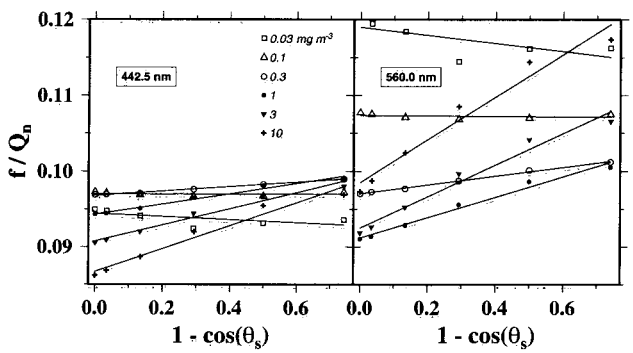

Fig. 20. Selected examples of computed f/Q_n values plotted as a function of $(1 - \cos\theta_s)$ and corresponding linear fit (Table 3).

water-leaving radiance; with the nadir-viewing strategy, Eq. (13) simplifies to

$$[L_w]_N^{ex} = [L_w]_N \frac{f_0(\text{Chl}, \lambda)}{Q_0(\text{Chl}, \lambda)} \left(\frac{f(\theta_s, \text{Chl}, \lambda)}{Q_n(\theta_s, \text{Chl}, \lambda)} \right)^{-1}, \quad \text{(B3)}$$

where W and τ_a are omitted, and the above relationships [Eqs. (B1) and (B2)] can be directly used to perform the transformation. Considering these expressions and the fact that f and Q are associated through their ratio, it is logical to seek a similar relationship directly involving this ratio and having the form

$$(f/Q_n)(\theta_s, \lambda, \text{Chl}) = (f_0/Q_0)(0, \lambda, \text{Chl}) + S_{f/Q}(\lambda, \text{Chl})(1 - \cos\theta_s). \quad \text{(B4)}$$

The fit of the results on this equation is actually possible, and the validity of the linear approximations (Fig. 20) can be considered as acceptable, even as great as $\theta_s = 75°$. However, the goodness of the fit deteriorates slightly, compared with those obtained separately for Eqs. (B1) and (B2); the relative errors expected from the use of Eq. (B4) might reach ±3.4%. Table 3 provides the appropriate values of the initial f_0/Q_0 term and slopes $S_{f/Q}$. Note that these three equations and associated tables are based on computations that account for the Raman emission.

We are pleased to thank Michael Mishchenko for his advice and generous help when operating his T-matrix code for computing the scattering phase

Table 3. f_0/Q_0 Ratio and the Associated Slope of Its Relationship to the Cosine of the Sun Zenith Angle

Parameter	Wavelength (nm)						
f_0/Q_0 (mg m^{-3})	412.5	442.5	490	510	560	620	660
0.03	0.089538	0.094417	0.106584	0.112755	0.118970	0.118219	0.118756
0.1	0.095834	0.097003	0.101338	0.104170	0.107362	0.105764	0.104753
0.3	0.097576	0.096815	0.097281	0.097115	0.097048	0.094493	0.093036
1	0.095803	0.094307	0.094060	0.092853	0.091167	0.086045	0.084662
3	0.092191	0.090745	0.091792	0.091698	0.092447	0.082218	0.080325
10	0.087741	0.086690	0.089566	0.091422	0.098468	0.082820	0.078632
S_{f/Q_n} (mgm^{-3})							
0.03	−0.001395	−0.002067	−0.003802	−0.005239	−0.005314	−0.005261	−0.005363
0.1	−0.000254	−0.000101	0.000308	−0.000721	−0.000318	−0.000162	0.000289
0.3	0.001678	0.002867	0.005181	0.004966	0.005726	0.004667	0.005080
1	0.004727	0.006759	0.010777	0.011601	0.013461	0.009248	0.008975
3	0.008255	0.010688	0.015709	0.017363	0.020826	0.015052	0.013596
10	0.012713	0.015235	0.021056	0.023357	0.028172	0.023455	0.020462

functions by spheroidal particles. We are indebted to M. Lewis for helpful suggestions and comments on a first draft of this paper and Bryan Franz for testing the effects of these bidirectional corrections upon the SeaWiFS data. We thank four anonymous reviewers for their useful comments and suggestions. This study was supported by the European Space Agency under contract ESA-ESTEC/14558/00/NL/DC.

References and Notes

1. A. Morel and B. Gentili, "Diffuse reflectance of oceanic waters: its dependence on Sun angle as influenced by the molecular scattering contribution," Appl. Opt. **30,** 4427–4438 (1991).
2. A. Morel and B. Gentili, "Diffuse reflectance of oceanic waters. II. Bidirectional aspects," Appl. Opt. **32,** 6864–6879 (1993).
3. A. Morel and B. Gentili, "Diffuse reflectance of oceanic waters. III. Implication of bidirectionality for the remote-sensing problem," Appl. Opt. **35,** 4850–4862 (1996).
4. K. J. Voss, "Electro-optic camera system for measurement of the underwater radiance distribution," Opt. Eng. **28,** 241–247 (1989).
5. A. Morel, K. J. Voss, and B. Gentili, "Bidirectional reflectance of oceanic waters: a comparison of modeled and measured upward radiance fields," J. Geophys. Res. **100,** 13143–13151 (1995).
6. H. Loisel and A. Morel, "Non-isotropy of the upward radiance field in typical coastal (Case 2) waters," Int. J. Remote Sens. **22,** 275–295 (2001).
7. T. J. Petzold, "Volume scattering functions for selected ocean waters," Rep. 510, Ref. 72–78 (Scripps Institution of Oceanography, La Jolla, Calif., 1972).
8. C. D. Mobley, B. Gentili, H. R. Gordon, Z. Jin, G. W. Kattawar, A. Morel, P. Reinersman, K. Stamnes, and R. H. Stavn, "Comparison of numerical models for computing underwater light fields," Appl. Opt. **32,** 7884–7504 (1993).
9. J. T. O. Kirk, "Dependence of relationship between inherent and apparent optical properties of water on solar altitude," Limnol. Oceanogr. **29,** 350–356 (1984).
10. H. R. Gordon, "Dependence of the diffuse reflectance of natural waters on the sun angle," Limnol. Oceanogr. **34,** 1484–1489 (1989).
11. A. Morel and S. Maritorena, "Bio-optical properties of oceanic waters: a reappraisal," J. Geophys. Res. **106,** 7163–7180 (2001).
12. H. R. Gordon, O. B. Brown, R. H. Evans, J. W. Brown, R. C. Smith, K. S. Baker, and D. K. Clark, "A semi-analytic radiance model of ocean color," J. Geophys. Res. **93,** 10909–10924 (1988).
13. A. Morel, "Optical modeling of the upper ocean in relation to its biogenous matter content (Case 1 waters)," J. Geophys. Res. **93,** 10749–10768 (1988).
14. O. Ulloa, S. Sathyendranath, and T. Platt, "Effect of the particle-size distribution on the backscattering ratio in seawater," Appl. Opt. **33,** 7070–7077 (1994).
15. M. S. Twardowski, E. Boss, J. B. Macdonald, W. S. Pegau, A. H. Barnard, and R. V. Zaneveld, "A model for estimating bulk refractive index from the optical backscattering ratio and the implications for understanding particle composition in Case I and Case II waters," J. Geophys. Res. **106,** 14129–14142 (2001).
16. H. R. Gordon and O. B. Brown, "A theoretical model of light scattering by Sargasso Sea particulates," Limnol. Oceanogr. **17,** 826–832 (1972).
17. O. B. Brown and H. R. Gordon, "Two component Mie scattering models of Sargasso Sea particles," Appl. Opt. **12,** 2461–2465 (1973).
18. J. R. V. Zaneveld, D. M. Roach, and H. Pak, "The determination of the index of refraction distribution of oceanic particulates," J. Geophys. Res. **79,** 4091–4095 (1974).
19. O. V. Kopelevich, "Small parameter model of optical properties of seawater," in *Ocean Optics*, A. S. Monin, ed. (Nauka, Moscow, 1983), Vol. 1, Chap. 8 (in Russian).
20. K. S. Shifrin, *Physical Optics of Ocean Water* (American Institute of Physics, New York, 1988).
21. C. D. Mobley, *Light and Water: Radiative Transfer in Natural Waters* (Academic, San Diego, Calif., 1994).
22. V. I. Haltrin and G. Kattawar, "Light fields with Raman scattering and fluorescence in sea water," Tech. Rep. (Department of Physics, Texas A & M University, College Station, Texas, 1991).
23. D. Stramski and D. A. Kiefer, "Light scattering by microorganisms in the open ocean," Prog. Oceanogr. **28,** 343–383 (1991).
24. E. Aas, "Refractive index of phytoplankton derived from its metabolite composition," J. Plankton Res. **18,** 2223–2248 (1996).
25. H. Claustre, A. Morel, S. B. Hooker, D. Antoine, K. Oubelkheir, A. Bricaud, K. Leblanc, B. Queginer, and S. Maritorena, "Is desert dust making oligotrophic waters greener?" Geophys. Res. Lett. **29,** 10.1029/2001GL014056 (2002).
26. M. I. Mishchenko, L. D. Travis, and D. W. Mackowski, "*T*-matrix computations of light scattering by nonspherical particles: a review," J. Quant. Spectrosc. Radiat. Transfer **55,** 535–575 (1996).
27. A. Morel, "Optical properties of pure water and pure sea water," in *Optical Aspects of Oceanography*, N. G. Jerlov and E. S. Nielsen, eds. (Academic, New York, 1974), Chap. 1.
28. H. Loisel and A. Morel, "Light scattering and chlorophyll concentration in Case 1 waters: a reexamination," Limnol. Oceanogr. **43,** 847–858 (1998).
29. H. R. Gordon and D. K. Clark, "Clear water radiances for atmospheric correction of coastal zone color scanner imagery," Appl. Opt. **20,** 4175–4180 (1981).
30. C. Cox and W. Munk, "Some problems in optical oceanography," J. Mar. Res. **14,** 63–78 (1955).
31. W. W. Gregg and K. L. Carder, "A simple spectral solar model for cloudless maritime atmospheres," Limnol. Oceanogr. **35,** 1657–1675 (1990).
32. J. S. Bartlett, K. J. Voss, S. Sathyendranath, and A. Vodacek, "Raman scattering by pure water and seawater," Appl. Opt. **37,** 3324–3332 (1998).
33. H. Neckel and D. Labs, "The solar radiation between 3300 and 12500 Å," Sol. Phys. **90,** 205–258 (1984).
34. J. L. Mueller and G. S. Fargion, eds., "Ocean optics protocols for satellite ocean color sensor validation, revision 3," (NASA Goddard Space Flight Center, Greenbelt, Md., 2002).
35. J. E. Tyler, "Radiance distribution as a function of depth in a underwater environment," Bull. Scripps Inst. Oceanogr. **7,** 363–412 (1960).
36. J. E. Tyler and R. W. Preisendorfer, "Transmission of energy within the sea," in *The Sea*, M. N. Hill, ed. (Wiley-Interscience, New York, 1962), Vol. 1, pp. 397–448.
37. E. Aas and N. K. Hojerslev, "Analysis of underwater radiance observations: apparent optical properties and analytic functions describing the angular radiance distribution," J. Geophys. Res. **104,** 8015–8024 (1999).
38. G. Zibordi and J.-F. Berthon, "Relationship between the *Q*-factor and seawater optical properties in a coastal region," Limnol. Oceanogr. **46,** 1130–1140 (2001).
39. SeaWiFS (Orbital Sciences Corp., NASA) is an ocean color sensor, operating since September 1997. See also S. B. Hooker, W. E. Esaias, G. C. Feldman, W. W. Gregg, and C. R. McClain, "An overview of SeaWiFS and ocean color," NASA Tech. Memo. 104566 **1,** S. B. Hooker and E. R. Firestone, eds. (NASA Goddard Space Flight Center, Greenbelt, Md., 1992).
40. The PROSOPE cruise (4 September–4 October 1999), on board the research vessel Thalassa, started in Agadir, Morocco, and ended in Toulon, France.